applied sciences

Article

Radiation-Induced Thermal Runaway Propagation in a Cylindrical Li-Ion Battery Pack: Non-Monotonicity, Chemical Kinetics, and Geometric Considerations

Liwen Zhang [1], Yi Chen [2], Haiwen Ge [3], Ankur Jain [4] and Peng Zhao [1,*]

[1] Department of Mechanical, Aerospace and Biomedical Engineering, UT Space Institute, University of Tennessee, Knoxville, TN 37388, USA; lzhan110@vols.utk.edu
[2] Magna Powertrain of America, Inc., Troy, MI 48083, USA; yi.chen2@magna.com
[3] Zhejiang Lab., Hangzhou 311121, China; gehaiwen@zhejianglab.com
[4] Department of Mechanical and Aerospace Engineering, University of Texas at Arlington, Arlington, TX 76019, USA; jaina@uta.edu
* Correspondence: pzhao12@utk.edu

Abstract: Li-ion batteries play a key role in energy storage and conversion in engineering systems such as electric vehicles and grid energy storage, with critical impact on electrification and storage of renewable energy. A key unresolved technological challenge in Li-ion batteries pertains to thermal runaway initiation and propagation in a battery pack, which can lead to subsequent fire and explosion. Despite significant past work, there remains a critical need to understand how thermal runaway propagates in a pack. This work presents a comprehensive investigation of the effect of radiative heat transfer on thermal runaway propagation. Radiation can be important when a battery is exposed to adjacent heat and fire sources, as well as in thermal runaway propagation from one hot cell to another. A theoretical radiative heat transfer model based on view factor theory is developed. Calculations based on this model for a simple 2D cylinder-to-cylinder geometry are found to be in very good agreement with analytical expressions. Radiation-induced thermal runaway propagation between two cylindrical 18650 batteries is evaluated. It is shown that radiation may play a key role in thermal runaway propagation, depending strongly on the triggering temperature. It is found that radiative effects in thermal runaway propagation exhibit both nonlinear and non-monotonic characteristics. At high temperatures, thermal runaway is triggered rapidly in the region close to the battery surface, where the chemical reactions are strongly coupled, and radiation plays a dominant role. In contrast, at lower temperatures, thermal runaway is triggered much more slowly and towards the core of the cell, where some chemical reactions may be decoupled, and pre-runaway chemical heat release plays an increasingly important role. The results presented here suggest that radiation can either facilitate or mitigate thermal runaway. The net radiation heat flux has a cross-over instant, beyond which radiation starts to retard thermal runaway. Additionally, the blocking effect in radiative heat transfer between cells arranged in equal-spacing homogenous or orthogonal arrangements in a battery pack is investigated, along with the effect of the hot spot size. Results from this work help understand the role of radiation in thermal runaway propagation and provide useful insights into the thermal runaway control and design of safe Li-ion battery packs.

Keywords: radiation; thermal runaway; Li-ion battery; energy storage; thermal runaway propagation; view factor

check for updates

Citation: Zhang, L.; Chen, Y.; Ge, H.; Jain, A.; Zhao, P. Radiation-Induced Thermal Runaway Propagation in a Cylindrical Li-Ion Battery Pack: Non-Monotonicity, Chemical Kinetics, and Geometric Considerations. *Appl. Sci.* **2023**, *13*, 8229. https://doi.org/10.3390/app13148229

Academic Editor: In Sun Cho

Received: 6 May 2023
Revised: 5 July 2023
Accepted: 13 July 2023
Published: 15 July 2023

1. Introduction

Li-ion battery (LIB) technology has attracted extensive research interest, as it offers an efficient mechanism for energy conversion and storage, thus contributing towards decarbonization and energy electrification [1]. LIBs offer very high conversion efficiency between chemical and electrical energy. If the electricity comes from clean and renewable energy resources, LIB technology with sufficiently long cycle life will not further increase the carbon footprint from electricity generation and utilization. Moreover, LIBs can be seamlessly integrated with existing infrastructure and ongoing efforts in the energy sector—for example, the electricity grid, centralized carbon capture and sequestration, etc. Li-ion battery-based energy storage systems include large-scale Li-ion battery packs with additional control and thermal management modules, which enable load-shifting, frequency regulation, long-term storage, and decentralized deployment. In addition, LIB-based energy storage systems facilitate synergistic integration of other technologies toward decarbonization, such as battery regeneration and material recycling. Through the combination of existing grid infrastructure, diversified power generation, centralized carbon capture and sequestration, increased renewable energy, and efficient battery regeneration, a clean and sustainable energy sector can be expected in the future with LIB-based energy storage systems.

However, the operation of LIBs is extremely sensitive to temperature. Thermal runaway and subsequent fires can be triggered when LIBs are exposed to abuse conditions such as overheating [2,3], internal short circuit [4,5], collision, and nail penetration [6,7]. Thermal runaway of LIBs has attracted extensive research interest in the recent past. These research efforts include characterization of the thermal stability of battery materials [8,9], battery and pack-level thermal runaway testing [10,11], development of kinetic models of thermal runaway [12,13], optimized cooling system design to mitigate thermal runaway and its propagation [14–18], modelling and simulation of thermal runaway using detailed and reduced-order models [19,20], and venting gas generation and subsequent fires [21–23].

Figure 1 shows the thermal runaway mechanism in a typical LIB with a $LiCoO_2$ cathode, an electrolyte of ethylene carbonate ($C_3H_4O_3$) and lithium hexafluorophosphate ($LiPF_6$), and a graphite anode. The solid electrolyte interphase (SEI) layer is thermally unstable and can decompose when subjected to high temperature or other abuse. The lithium in the anode will then directly contact the electrolyte and form lithium carbonate and ethylene. In addition, the cathode and electrolyte can directly react through the oxygen generated from cathode decomposition. Finally, the electrolyte material carbonate and salt can decompose under elevated temperatures. These reactions are largely exothermic and accompanied by the formation of gases such as ethylene and oxygen, thereby creating a self-sustained, destructive chain of highly exothermic reactions.

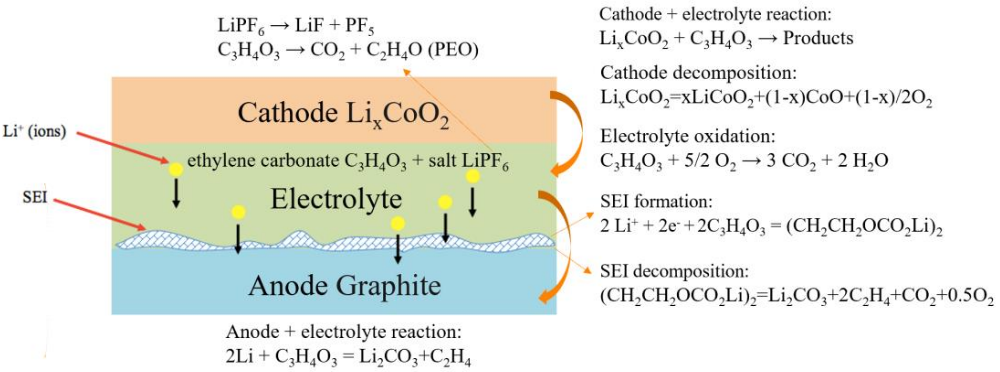

Figure 1. Configuration and thermal runaway reactions for a typical LCO LIB.

Understanding the factors that impact the propagation of thermal runaway in a large battery pack remains an important research challenge. Past work has shown that multiple factors including cell-to-cell gap, thermal properties of the interstitial material, and kinetics of the decomposition reactions all play a key role in determining whether thermal runaway propagation occurs or not [24]. However, the role of radiative heat transfer in thermal runaway propagation has remained poorly understood, primarily due to the strong nonlinearity of radiation and its coupling with thermal runaway chemistry. Radiative heat transfer is usually dominant in high-temperature processes, such as combustion, which are, in principle, similar to thermal runaway. In the context of Li-ion cells, radiation is known to play a critical role in increasing the battery temperature and activating thermal runaway reactions [25–30]. The role of radiation in thermal runaway propagation in a pack of cylindrical cells has been investigated computationally [31]. These results have shown that neglecting radiation leads to a prediction of onset in the trigger battery but an erroneous prediction of no thermal runaway propagation. In addition, thermal radiation has often been combined with the effects of conduction and convection in studying the triggering of thermal runaway [30,32], leading to ambiguity on the specific role of radiative heat transfer. A radiative shielding method to minimize thermal runaway propagation has been presented, where the fraction of heat flux due to radiation in a battery pack during thermal runaway is also evaluated [33]. More recently, our experiments have demonstrated battery-to-battery variability in thermal runaway [34], even among batteries with the same chemistry and near-identical initial conditions. It is hence expected that variation from radiation in the triggering cell can lead to different modes and paths for thermal runaway propagation in a pack, which necessitates study on the specific role of radiative heat transfer.

The literature cited above clearly highlights the importance of radiative heat transfer and the need for a comprehensive investigation of how radiative heat transfer impacts thermal runaway propagation. This work presents an investigation of the role of radiative heat transfer in thermal runaway propagation when an LIB is exposed to fire and other heat sources. A limiting condition for triggering thermal runaway by radiative heat transfer between two closely packed cylindrical cells is computationally investigated. Results indicate the existence of complex nonlinear coupling between chemical reactions and thermal radiation. A key novelty of the work is that we have identified the non-monotonic impact of radiation on thermal runaway triggering and have mapped out the regime diagram under both low- and high-temperature limits. We have shown that, depending on conditions, radiation can either facilitate or mitigate thermal runaway. When the triggering cell is at a relatively low temperature, we have further shown that pre-runaway chemistry plays an increasingly significant role. We extend our investigation to battery packs and practical conditions where radiative blocking effects and localized hot spots may be important. Results presented here highlight the importance of radiative heat transfer in thermal runaway propagation and can help guide future efforts towards mitigation of thermal runaway in safe electrochemical energy storage systems.

2. Materials and Methods

In this study, a 2D model is developed in COMSOL Multiphysics 5.5, where the heat transfer module is used to implement surface-to-surface radiation. Figure 2a shows a schematic of a typical pack of multiple, orthogonally arranged Li-ion cells with equal spacing. In general, the interest here is to understand how radiative heat transfer may facilitate the propagation of thermal runaway from one cell to the other. While the general problem comprising a number of cells is considerably complicated, for simplicity, the radiative exchange between a cell and one of its neighbors is considered first. The problem of radiation-induced thermal runaway between two neighboring cells may be treated as a 2D radiation heat transfer problem between two equal cylinders, as shown in Figure 2b.

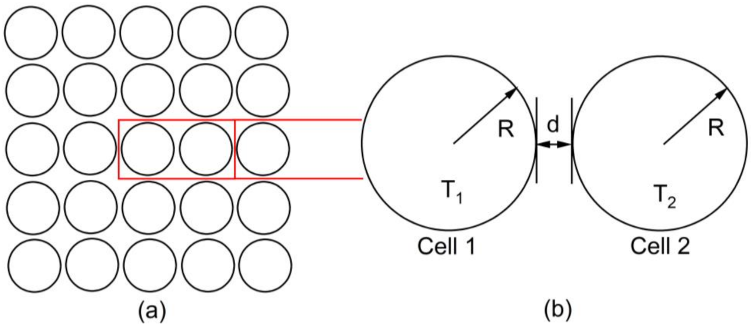

Figure 2. Schematic of simulation geometry of (**a**) a common configuration of cylindrical pack (**b**) two equal cylinders with radius R and separation d.

In order to understand how these two cells exchange heat radiatively, the general energy conservation equation is first written. Thermal conduction in the axial direction is ignored, since a typical cylindrical cell has a high aspect ratio. The transient differential equation that balances heat conduction in the axial and azimuthal directions as well as thermal runaway chemical heat release is given by:

$$\rho c_p \frac{\partial T}{\partial t} = \frac{1}{r}\frac{\partial}{\partial r}\left(k_r r \frac{\partial T}{\partial r}\right) + \frac{1}{r^2}\frac{\partial}{\partial \theta}\left(k_\theta \frac{\partial T}{\partial \theta}\right) + Q \tag{1}$$

where $t, r, \theta, \rho, c_p, T, k_r, k_\theta$, and Q are time, radial coordinate, angular coordinate, battery density, heat capacity, radial thermal conductivity, azimuthal thermal conductivity, and heat generation within the battery, respectively. Based on previous work [34], the values of thermophysical properties of a typical Li-ion cell are provided in Table 1. Considering the jellyroll-layered structure of a cylindrical cell, the azimuthal in-plane thermal conductivity is much higher compared to the out-of-plane radial thermal conductivity. As such, the limiting heat conduction that is essential for thermal runaway initiation is in the radial direction. For these considerations, the problem is simplified as a 2D limiting condition with both k_r and k_θ having equal out-of-plane thermal conductivity.

Table 1. Model parameters in the thermal radiation model [34].

Parameter (Unit)	Value
Battery radius, R (mm)	9
Battery density, ρ $\left(\text{kg/m}^3\right)$	2060
Heat capacity, c_p $(\text{J/kg}\cdot\text{K})$	1000
Radial thermal conductivity, k $(\text{W/m}\cdot\text{K})$	0.8

The heat generation term Q originates from four well-known semi-global thermal runaway chemical reactions [12]. These exothermic reactions include the solid–electrolyte–interface decomposition reaction, the anode–electrolyte reaction, the cathode–electrolyte reaction, and the electrolyte decomposition. The rates of these reactions depend on the battery material properties, thermal chemical parameters, and the battery temperature. The reaction model, frequency factor, and activation energy that describe the kinetics between the electrolyte and electrode materials have been previously obtained by fitting the experimental measurements from accelerating rate calorimetry (ARC) and differential scanning calorimetry (DSC) tests. Expressions for the chemical reaction rates and heat generation rates for these reactions are shown in Tables 2 and 3, with symbols and parameter values used here as in our previous work [35,36]. The present model for LCO thermal runaway chemistry is capable of accounting for more complicated reaction models and other cathode chemistry.

Table 2. Heat generation from side chemical reactions equations of thermal abuse model [35,36].

Reaction term	Equations	
SEI decomposition	$\frac{dc_{sei}}{dt} = -A_{sei}exp\left[-\frac{E_{a,sei}}{RT}\right]c_{sei}^{m_{sei}}$	$Q_{sei} = -H_{sei}W_c\frac{dc_{sei}}{dt}$
Anode–electrolyte reaction	$\frac{dc_{ne}}{dt} =$ $-A_{ne}exp\left[-\frac{t_{sei}}{t_{sei0}}\right]c_{ne}^{m_{ne}}exp\left[-\frac{E_{a,ne}}{RT}\right]\frac{dt_{sei}}{dt} =$ $A_{ne}exp\left[-\frac{t_{sei}}{t_{sei0}}\right]c_{ne}^{m_{ne}}exp\left[-\frac{E_{a,ne}}{RT}\right]$	$Q_{ne} = -H_{ne}W_c\frac{dc_{ne}}{dt}$
Cathode–electrolyte reaction	$\frac{d\alpha}{dt} = A_{pe}\alpha^{m_{pe1}}(1-\alpha)^{m_{pe2}}exp\left[-\frac{E_{a,pe}}{RT}\right]$	$Q_{pe} = -H_{pe}W_p\frac{d\alpha}{dt}$
Electrolyte decomposition	$\frac{dc_e}{dt} = -A_e exp\left[-\frac{E_{a,e}}{RT}\right]c_e^{m_e}$	$Q_e = -H_eW_e\frac{dc_e}{dt}$
Overall heat generation	$Q = Q_{sei} + Q_{ne} + Q_{pe} + Q_e$	

Table 3. Thermochemical parameters adopted in the thermal runaway model of $LiCoO_2$/graphite battery [35,36].

Symbol	Equations	Physical Description
A_{sei}	1.667×10^{15} (1/s)	SEI–decomposition frequency factor
A_{ne}	2.5×10^{13} (1/s)	Anode–electrolyte frequency factor
A_{pe}	6.667×10^{13} (1/s)	Cathode–electrolyte frequency factor
A_e	5.14×10^{25} (1/s)	Electrolyte decomposition frequency factor
$E_{a,sei}$	1.3508×10^5 (J/mol)	SEI–decomposition activation energy
$E_{a,ne}$	1.3508×10^5 (J/mol)	Anode–electrolyte activation energy
$E_{a,pe}$	1.396×10^5 (J/mol)	Cathode–electrolyte activation energy
$E_{a,e}$	2.74×10^5 (J/mol)	Electrolyte decomposition activation energy
c_{sei0}	0.15	Initial value of c_{sei}
c_{ne0}	0.75	Initial value of c_{ne}
α_0	0.04	Initial value of α
c_{e0}	1	Initial value of c_e
t_{sei0}	0.033	Initial value of t_{sei}
m_{sei}	1	Reaction order for c_{sei}
m_{ne}	1	Reaction order for c_{ne}
m_{pe1}	1	Reaction order for α
m_{pe2}	1	Reaction order for $1 - \alpha$
m_e	1	Reaction order for c_e
H_{sei}	2.57×10^5 (J/kg)	Reaction heat of SEI–decomposition
H_{ne}	1.714×10^6 (J/kg)	Reaction heat of anode–electrolyte
H_{pe}	3.14×10^5 (J/kg)	Reaction heat of cathode–electrolyte
H_e	1.55×10^5 (J/kg)	Reaction heat of electrolyte decomposition
W_c	6.104×10^2 (kg/m^3)	Specific carbon content in jellyroll
W_p	1.221×10^3 (kg/m^3)	Specific positive active content in jellyroll
W_e	4.069×10^2 (kg/m^3)	Specific electrolyte content in jellyroll
$\bar{R}$	8.314 (J/mol/K)	Universal gas constant

At the surface, thermal radiation is considered exclusively, and convective effects are ignored. This corresponds to the practical condition in a pack where there is no forced convective flow and the radiation heat transfer dominants. A schematic diagram of radiative heat exchange between the two cells is shown in Figure 3. The radiation heat flux emitted from Cell 1 is the irradiation G:

$$G = \varepsilon\sigma {T_1}^4 \tag{2}$$

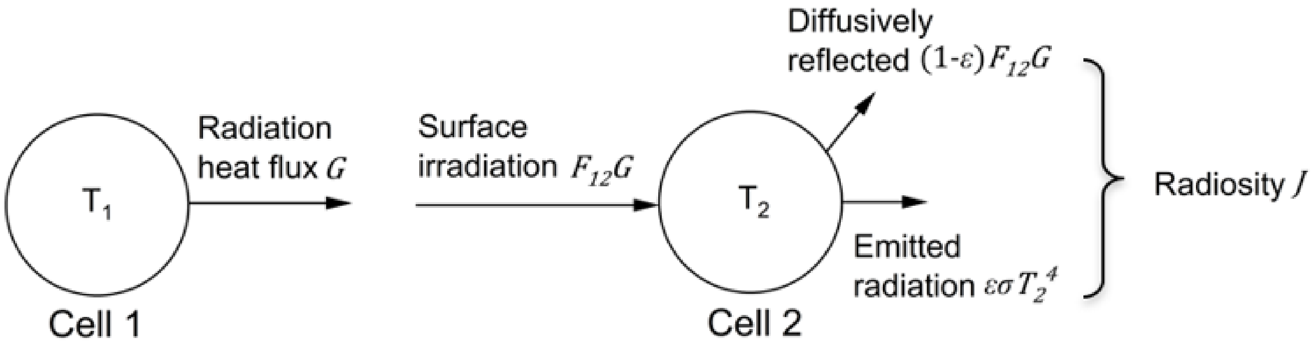

Figure 3. Schematic of thermal radiation between two equal external cylindrical cells.

For Cell 2, we can define the radiosity J, the radiation heat flux leaving its surface:

$$J = \varepsilon\sigma {T_2}^4 + (1 - \varepsilon)F_{12}G \tag{3}$$

where the radiosity has been expressed as the sum of diffusively reflected and emitted radiation from Cell 2. Consequently, the net radiation heat flux on Cell 2 can be written as:

$$q = F_{12}G - J \tag{4}$$

In these equations, ε is the emissivity, σ is the Stefan–Boltzmann constant, T_1 is the temperature of Cell 1, T_2 is the temperature of Cell 2, T_{amb} is ambient temperature, and F_{12} is the view factor from Cell 1 to Cell 2.

In order to validate the thermal radiation modelling, a quasi-steady state radiative heat transfer problem between two equal cylinders of radius R = 9 mm is considered. With the given separation distance and cylinder temperatures, we can numerically simulate the radiation heat flux received by Cell 2 among the total radiation emitted from Cell 1, that is, GF_{12}. Meanwhile, in classical heat transfer theory, the radiation heat flux between two cylinders is analytically available with a known view factor, which can be used to validate the simulation results. The view factor between two equal cylinders has been derived from the view factor for general parallel cylinders as follows [37]:

$$F_{12} = \frac{\sqrt{\left(\frac{2R+d}{R}\right)^2 - 4} - \frac{2R+d}{R} + 2arcsin\left(\frac{2R}{2R+d}\right)}{2\pi} \tag{5}$$

As shown in Figure 4a,b, the numerical radiation heat flux is compared with the analytical theory between two equal blackbody cylinders (i) with fixed temperature but varying distance and (ii) with fixed distance but varying temperature of the Cell 1. The results suggest that as the distance of two cells increases, the radiation heat flux decreases. Also, as the temperature of Cell 1 increases, the radiation heat flux received by Cell 2 increases. The numerical calculation of the radiation heat flux is in excellent agreement with analytical results, further substantiating the simulation tool.

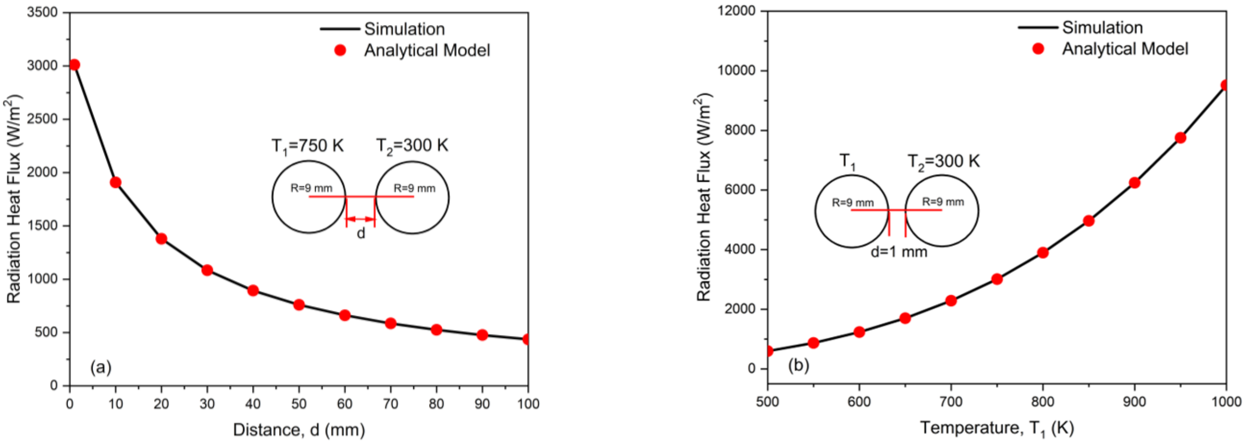

Figure 4. Validation of simulation results against analytical model for surface-to-surface radiation modeling: (**a**) Radiation heat flux vs. distance d between two cells with fixed cell temperatures. (**b**) Radiation heat flux vs. temperature T_1 of Cell 1 with fixed distance d and temperature T_2 of Cell 2.

In the thermal runaway simulation, we fix the temperature T_1 of Cell 1 and the ambient temperature (293 K) in each case. The initial temperature of Cell 2 is also taken to be 293 K. The evolution of T_2 is numerically solved by accounting for radiation, conduction, and thermal runaway chemical heat release based on Equation (1). The surface-to-surface radiation is simulated using the hemicube method. A time-dependent Multifrontal Massively Parallel Sparse (MUMPS) solver is used to solve for the thermal energy conservation equation. The backward differentiation formula (BDF) method is used for time stepping. The relative tolerance for the solution is 10^{-3}. Based on this general methodology, a number of investigations are carried out to understand the nature of radiation-induced thermal runaway, as well as the coupling between radiation and chemical heat generation. These results are discussed in the next section.

In the following (Sections 3.1–3.3), we have adopted a cell spacing d of 1 mm to investigate the feature of radiation-induced thermal runaway. There are two primary considerations behind the choice of cell separation d: energy density and safety. For energy considerations, the larger the cell spacing, the fewer number of cells can be accommodated in a given space, hence reducing the energy density of the pack. For safety, however, larger spacing is preferred, as thermal runaway propagation is less likely. As such, there is eventually a trade-off effect between these two considerations. Cell spacing of 1 mm in a battery pack has been adopted previously in [38–40]. Note that concepts and techniques developed in this work can also easily be applied to investigate radiative heat transfer for other cell spacing configurations.

3. Results and Discussions

3.1. General Features of Radiation-Induced Thermal Runaway

Figure 5a shows the evolution of maximum temperature of Cell 2 with different temperature of Cell 1, T_1. The results show that for $T_1 > 602$ K, thermal runaway occurs in Cell 2, as indicated by the sharp increase in T_2. For all these cases, the higher the T_1, the earlier the thermal runaway is triggered in Cell 2, as expected. When T_1 is increased to 900 K, the thermal runaway delay time is reduced to around 1 min. There is a sharp change in the nature of curves in Figure 5a when T_1 is below a threshold value of 602 K, wherein it is found that thermal runaway is not triggered in Cell 2, even at much longer times. The maximum temperature of Cell 2 in such cases is found to eventually reduce to around 450 K, where a quasi-thermal equilibrium is reached due to the balance between the net radiation heat flux and chemical heat generation.

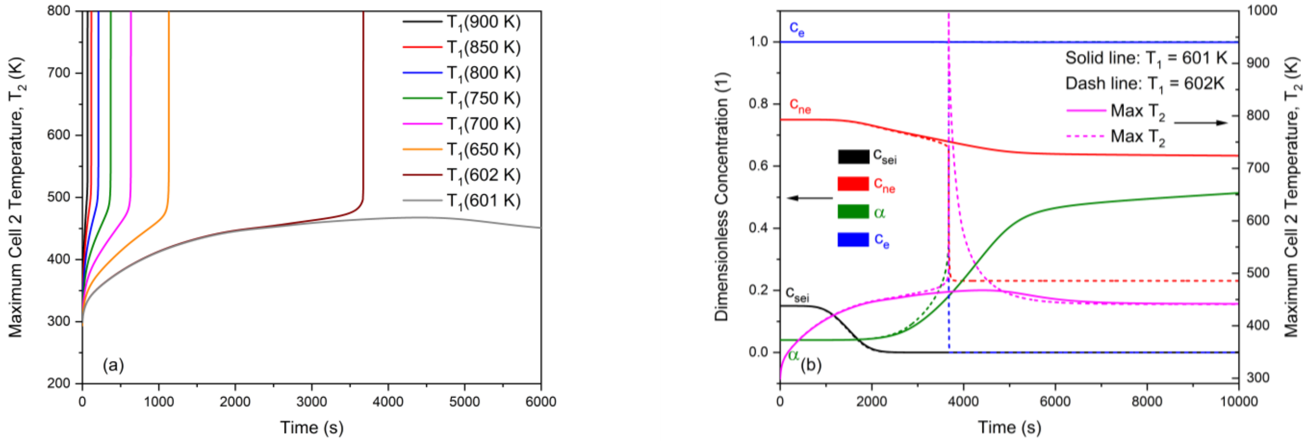

Figure 5. (**a**) Maximum temperature of Cell 2 as a function of time for different T_1. (**b**) Comparison of evolution of average dimensionless concentration and temperature for two cases close to the thermal runaway threshold T_1 = 601 K (solid lines) and T_1 = 602 K (dashed lines).

Figure 5b presents plots of T_2 as well as various dimensionless concentrations for two cases very close to the threshold found in Figure 5a: T_1 = 601 K and T_1 = 602 K. As shown in Figure 5b, the dimensionless SEI concentration is completely consumed around 2000 s for both T_1 = 602 K and 601 K cases, much earlier than the complete consumptions of other species, which occur at the instant of thermal runaway. Results suggest that the four chemical reactions may occur at different stages of thermal runaway, and their occurrence can be decoupled depending on the thermal runaway time scale. Evolution of the other dimensionless concentrations shows distinct behaviors, with much stronger consumption under thermal runaway conditions, as expected.

By defining the onset of thermal runaway as the instant with the maximum rate of temperature rise, Figure 6a,b plot spatial distributions of temperature and net heat generation rate, respectively, within Cell 2 at the onset of thermal runaway. It can be seen that the maximum temperature and peak heat release occurs in the vicinity of the surface of Cell 2 for high triggering temperature T_1 due to the large radiation heat flux from Cell 1. For extremely high T_1, the surface temperature of Cell 2 will rise so rapidly that thermal runaway will occur at or very close to the surface. Given that thermal runaway for high T_1 occurs so rapidly, as shown in Figure 5a, it is expected that radiation plays the sole dominant role for temperature rise during thermal runaway. At lower values of T_1, the location corresponding to the maximum temperature and peak heat release gradually moves to the internal region of the battery, indicating increased influence of heat conduction and heat generation from the chemical reactions during the much longer thermal runaway. For the threshold case with T_1 = 602 K, the peak heat release occurs very close to the center of Cell 2. The distinction between high T_1 and low T_1 behavior shown in Figure 6 can be explained by the increase of radiation time scales at reduced temperatures, where thermal conduction—a much slower, diffusive process—tends to play an increasingly significant role.

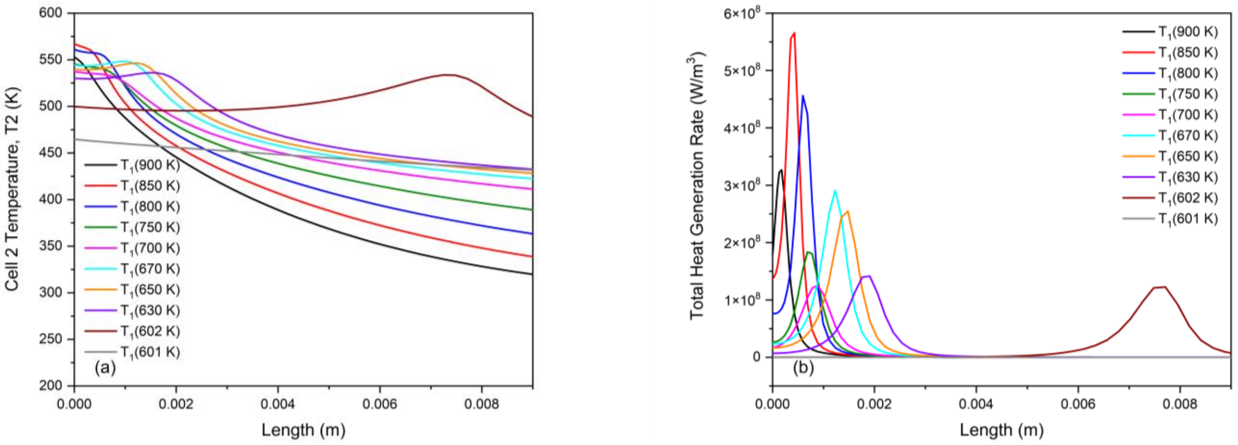

Figure 6. (**a**) Temperature distribution and (**b**) heat generation rate distributions within Cell 2 at the time of onset of thermal runaway for different values of T_1.

To further characterize the different thermal chemical processes for thermal runaway triggered by high and low temperature radiation, Figure 7 shows the evolution of dimensionless concentration and temperature in Cell 2 for a relatively high triggering temperature of T_1 = 900 K. Compared to the low triggering temperature case with T_1 = 602 K shown in Figure 5b, the thermal runaway is triggered much quicker. More interestingly, the mean dimensionless concentrations in the high temperature 900 K scenario do not exhibit obvious change before thermal runaway is triggered. The reactions are not separated in either spatial or time domain, and they tend to be activated simultaneously in the vicinity of the battery surface due to rapid radiative heating.

In summary, results so far demonstrate that radiation-induced onset of thermal runaway exhibits intrinsic differences depending on the triggering temperature: when T_1 is high, the thermal runaway is triggered very fast in the vicinity of the battery surface, and the thermal runaway reactions occur simultaneously in spatial and time. In such a case, radiation plays a solely dominant and direct role. In contrast, for low T_1, thermal runaway is triggered much slowly in the internal region of the battery, and the thermal runaway reactions can separate in spatial and time domains due to the depletion of certain species. In this case, radiation plays a less significant role.

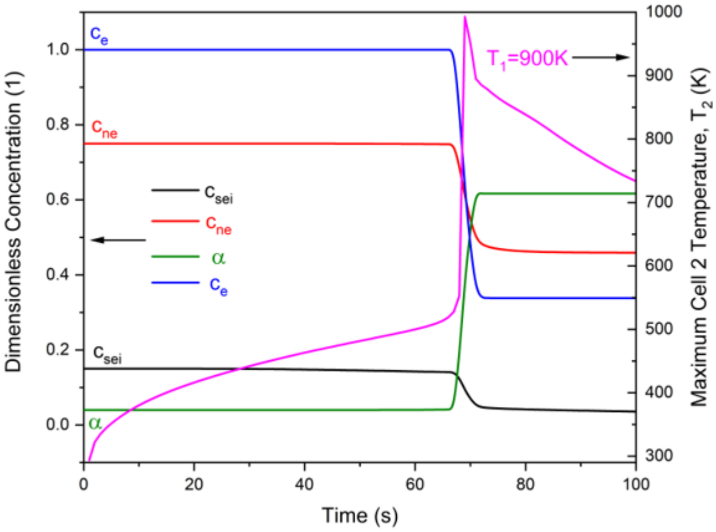

Figure 7. Evolution of average dimensionless concentration and temperature with thermal runaway triggering temperature of T_1 = 900 K.

3.2. Non-Monotonicity in Radiation-Induced Thermal Runaway

It should be noted that although Cell 2 receives radiation heat flux from Cell 1, it also emits radiation to the ambient. Therefore, at a certain state, the net radiation heat flux may become zero, even before thermal runaway occurs. In this scenario, the net radiation heat flux on Cell 2 can actually be negative, which may counteract the occurrence of thermal runaway. Figure 8 shows the evolution of net radiation heat flux q over the surface of Cell 2. It can be seen that for cases with T_1 = 602 K, q transitions to a negative value much earlier than the onset of thermal runaway, defined as the instant with maximum temperature rise rate. Therefore, in this case, radiation facilitates thermal runaway in the early stage before net radiation flux vanishes, and it actually mitigates thermal runaway in the later stage when net radiation flux becomes negative. With elevated temperature—when T_1 reaches close to 650 K—the cross-over state of q occurs very close to the onset of thermal runaway, indicating the constant promotion effects of radiation during thermal runaway at higher triggering temperatures.

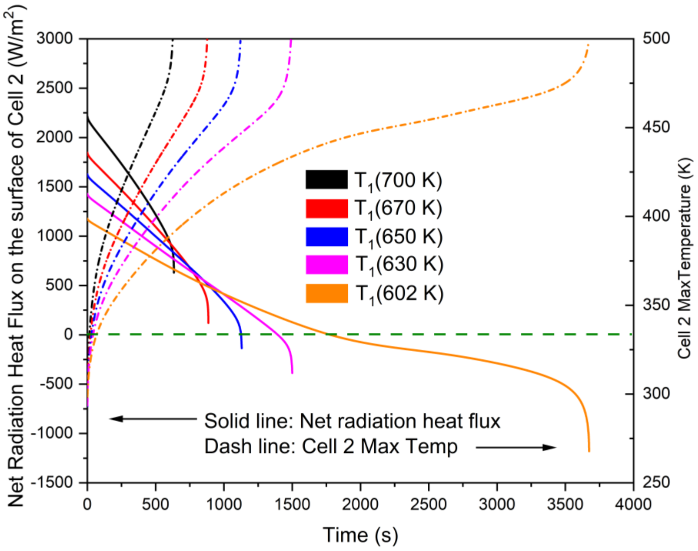

Figure 8. Evolution of net radiation heat flux q during thermal runaway with different T_1. Solid line is for net radiation heat flux over Cell 2 surface, dash dot is for the max temperature of Cell 2, green dash indicates the crossover of radiation heat flux.

To further characterize the role of radiative heat transfer at different triggering temperatures, a time-integrated radiative heat flux is calculated by integrating the net radiation flux q over the surface of Cell 2 from the initial condition to the instant of when the net radiation heat flux in Cell 2 vanishes. This provides a basis to evaluate the maximum facilitation effect of radiation on the triggering of thermal runaway. Interestingly, as shown in Figure 9, the time-integrated radiative heat flux as so defined exhibits a counter-intuitive non-monotonic dependence on temperature. On the high temperature branch, the integrated radiative heat flux decreases with increase in the triggering temperature, as expected. However, the peak-integrated radiative heat flux does not occur at the lowest temperature, as one might expect. Instead, it occurs at an intermediate temperature, around 700 K in this case. One possible explanation of such a non-monotonic trend may be offered by considering the time duration for the integral: higher triggering temperature T_1 leads to higher radiative heat flux, which nevertheless leads to a much shorter time scale to cancel out net radiation flux q. On the other hand, lower triggering temperature T_1 leads to lower radiative heat flux which, however, elongates the time scale to cancel out net radiation. This nevertheless only partially explains the role of radiation with varying triggering temperature, in that heat release from the exothermic thermal runaway reactions will also facilitate the temperature increment. With longer thermal runaway delay time at low temperatures, it allows longer residence time for the chemical reaction progress and heat release to accumulate internally within the cell.

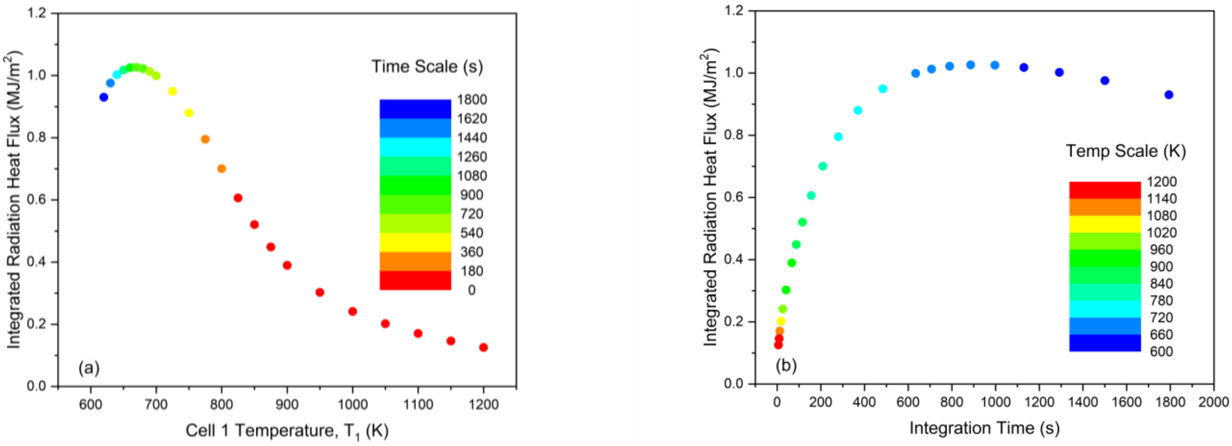

Figure 9. (**a**) Time-integrated net radiation heat flux at different triggering temperature; color indicates the time with zero net radiation flux. (**b**) Time-integrated net radiation heat flux versus integration time; color indicates thermal runaway triggering temperature.

3.3. Role of Pre-Runaway Chemical Heat Release in Radiation-Induced Thermal Runaway

To isolate the effect of chemical heat release before thermal runaway, Figure 10 compares the maximum temperature evolution of Cell 2 with and without the chemical heat source term included in the calculations. Results without chemical heat release represent contributions solely from radiation, while the difference between the cases with and without chemistry effectively represents the contribution from chemical heat release. We can select a temperature as the onset temperature of thermal runaway during the temperature rise—for example, 450 K or 500 K—and evaluate the temperature differences at these selected reference points. Figure 10a plots the temperature evolution with and without chemistry in high triggering temperature case T_1 = 900 K. At the reference onset temperature T_{ref} = 450 K, the temperature difference ΔT between the cases with and without chemistry is around 2.2 K, indicating the role of pre-runaway chemistry. Considering the total temperature rise at the reference $T_{ref} - T_{ini}$ = 450 − 293 = 157 K includes the combined effects of radiation and pre-runaway chemistry, the contribution of chemistry can therefore be reasonably isolated. Similarly, in the lower triggering temperature case shown in Figure 10b, the contribution of pre-runaway chemistry increases the battery temperature by 13.6 K, which is much higher compared to the higher triggering temperature case in Figure 10a.

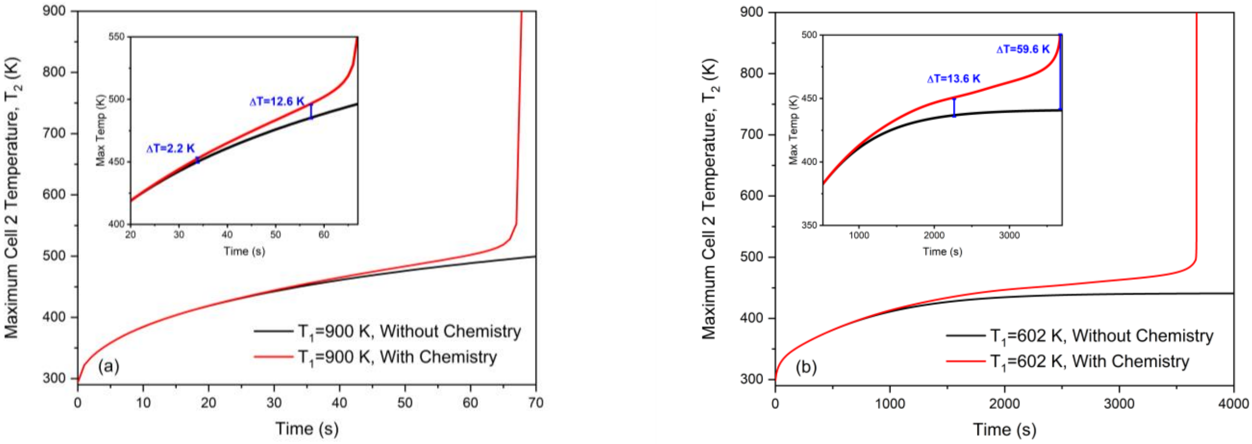

Figure 10. Temperature evolution with and without chemistry (**a**) in high triggering temperature T_1 = 900 K and (**b**) in low triggering temperature T_1 = 602 K, showing the role of heat release from pre-runaway chemistry.

The ratio of temperature rise from pre-runaway chemistry to the total temperature rise is evaluated at different triggering temperatures. It is shown in Figure 11 that at high triggering temperatures, the contribution of pre-runaway chemistry is very small: below 1% for T_{ref} = 450 K and below 5% for T_{ref} = 500 K. This indicates the sole dominant role of radiation for high temperature radiation-induced thermal runaway, while for the low triggering temperature conditions, the contribution of pre-runaway chemistry increases to around 10% for reference temperature 450 K and nearly 30% for onset reference temperature 500 K. The impact of pre-runaway chemistry becomes comparable to radiation and, hence, cannot be neglected.

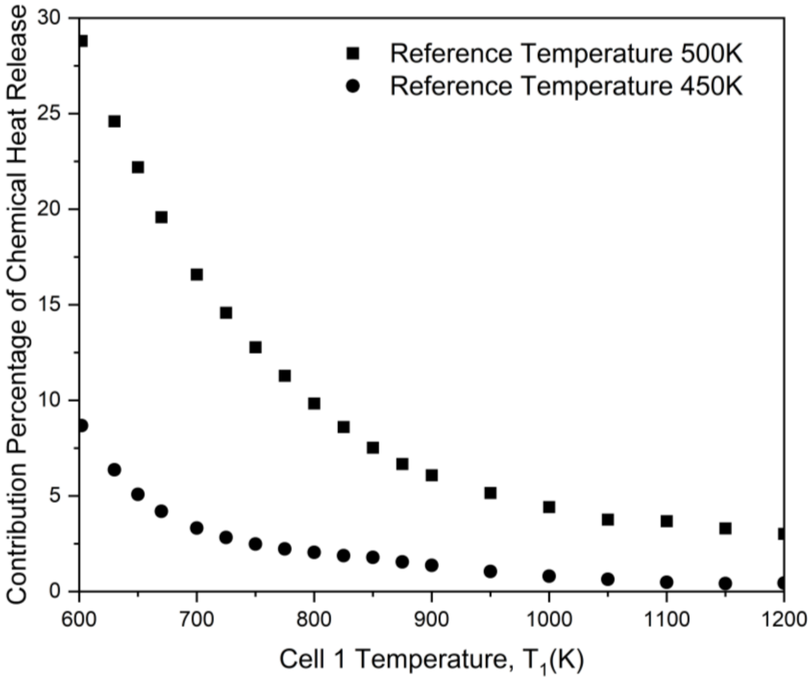

Figure 11. The contribution of chemical heat release during radiation-induced thermal runaway with different T_1.

3.4. Effects from Blockage on Radiation Heat Flux in Practical Battery Packs

In practical battery packs, depending on the separation distance d, thermal radiation from a trigger cell to another cell in the pack may be blocked by adjacent cells. For example, as shown by the schematic plot in Figure 12, radiation flux from O1 to O2 is blocked by the presence of O3, in that any photon emitted beyond point A on the surface of O1 is unable to directly reach the surface of O2. In general, the interest is in determining the extent of radiative exchange that will occur between any pair of cells in a battery pack, how this is influenced by the presence of other cells, and how the cells are arranged in the pack. Here, we considered two specific packing arrangements: equal-spacing homogenous or orthogonal.

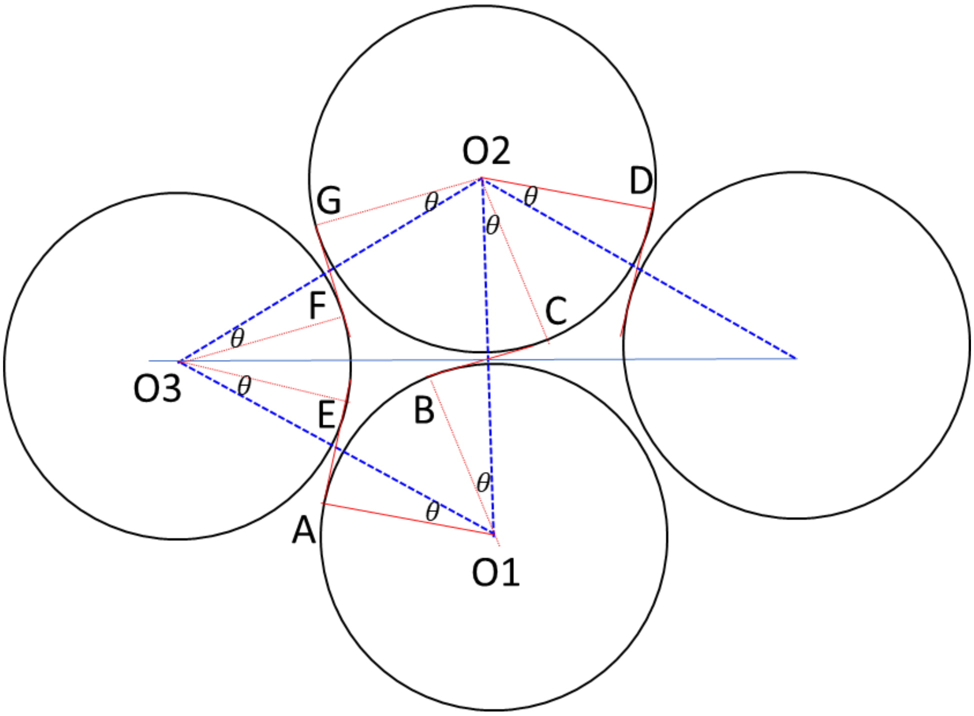

Figure 12. Schematic of a typical geometry where radiation flux between two equal cylinders O1 and O2 are blocked symmetrically by two extra equal cylinders, radius R and separation gap d.

Following Hotel's classical cross string theory [37], the view factor for arbitrary 2D geometry can be evaluated as:

$$F_{12} = \frac{\sum crossed\ strings - \sum uncrossed\ strings}{2 \times source\ string} \tag{6}$$

For the case of homogeneous arrangement of cells, we can express the view factor between Cells 1 and 2, F_{12} as:

$$\begin{aligned} F_{12} &= \frac{2\times\left(\hat{A}B+BC+C\hat{D}\right)-2\times\left(AE+E\hat{F}+FG\right)}{2\times2\pi R} \\ &= \frac{\left(\frac{2\pi R}{3}+2Rtan\theta\right)-\left(4Rtan\theta+R\left(\frac{\pi}{3}-2\theta\right)\right)}{2\pi R} \\ &= \frac{1}{6}-\frac{tan\theta}{\pi}+\frac{\theta}{\pi}=\frac{1}{6}-\frac{\sqrt{h^2-4}}{2\pi}+\frac{1}{\pi}arccos\frac{2}{h} \end{aligned} \tag{7}$$

Equations (5) and (7) can then be compared to understand the effect of blockage on radiation effect in a homogenously arranged battery pack, as demonstrated in Figure 13. As h = H/R approaches 2, the gap between each pair of cells approaches 0. This is the limit where the effect of blocking is most substantial, and it is shown that the difference of view factor and, hence, the radiation heat flux is as large as 8.2% with and without blockage. In the other limit with gradually increased cell separations, the effect from blockage gradually vanishes as expected, and hence Equations (5) and (7) reduce to the same results.

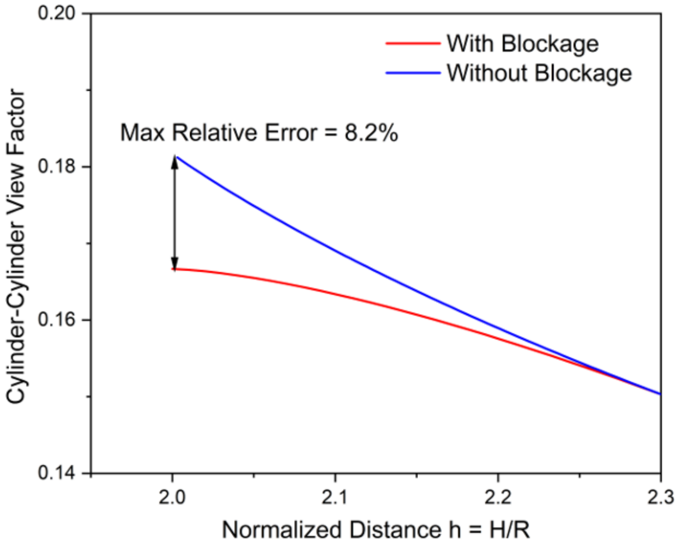

Figure 13. Comparison of view factors with and without the blockage between adjacent cells in equally spaced homogenous array.

Instead of being homogenously arranged, a more widely adopted practical real geometry of battery pack is the orthogonal configuration, as shown in Figure 14. Compared to the homogeneous arrangement, this configuration has reduced energy density for a given packing volume but provides more convenience for sequential and parallel electrical interconnection, as well as the provisioning of cooling. In this configuration, assuming the hot radiation source is the center Cell 5, the radiation heat flux from Cell 5 to any one of its immediate neighbors 2, 4, 6, and 8 is free of blockage, and, using Equation (5), the view factor may be written as

$$F_{52} = F_{54} = F_{56} = F_{58} = \frac{\sqrt{h^2-4} - h + 2arcsin\left(\frac{2}{h}\right)}{2\pi} \tag{8}$$

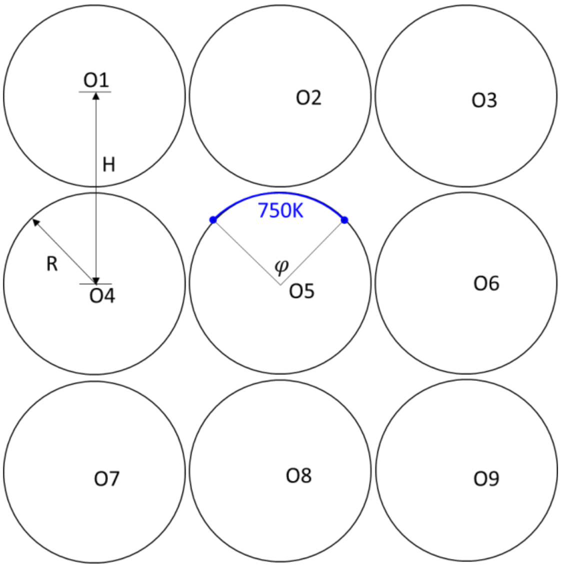

Figure 14. A common orthogonal arrangement of cylindrical battery packs with radius R and cell center distance H, h = H/R. O1 to O9 denote the center locations of each cell.

Radiative heat flux from the center Cell 5 to any one of the other Cells 1, 3, 7, and 9 can potentially be blocked, depending on the average separation among the cells. Due to symmetry, one can easily recognize that these view factors are equal:

$$F_{51} = F_{53} = F_{57} = F_{59} \tag{9}$$

Given the definition of view factor, the sum of view factor from Cell 5 to all reachable surfaces must be unity with sufficient small cell gaps. In other words, no radiation emission from Cell 5 is able to escape from all the cells around it. We hence can obtain:

$$F_{51} = F_{53} = F_{57} = F_{59} = \frac{1}{4} - \frac{\sqrt{h^2 - 4} - h + 2arcsin\left(\frac{2}{h}\right)}{2\pi} \tag{10}$$

With these view factors analytically obtained, the radiation heat flux from the center Cell 5 to all its adjacent cells with and without blockage can be easily evaluated. A comparison of the view factor in Equations (8) and (10) is presented in Figure 15, with Cells 2, 4, 6, and 8 as the closest cells relative to the trigger Cell 5, and 1, 3, 7, and 9 being next-closest cells. It is very interesting to see that there is a threshold cell separation distance h~2.7, within which the closest cells receive higher radiation while beyond which the corner cells receive higher radiation. For 18650 cell arrays, this limiting aspect ratio of h = 2.7 corresponds to a cell gap of 6.3 mm. In the other limit of h = 2, where cells directly touch with their closest neighbors, the radiation heat flux on the closest neighboring cell is more than two times higher than that received by the corner ones. With gradually increased spacing, the radiation heat flux drops on the closest cells and increases on the corner cells. This provides direct guidance on battery arrangement in arrays in order to suppress thermal runaway.

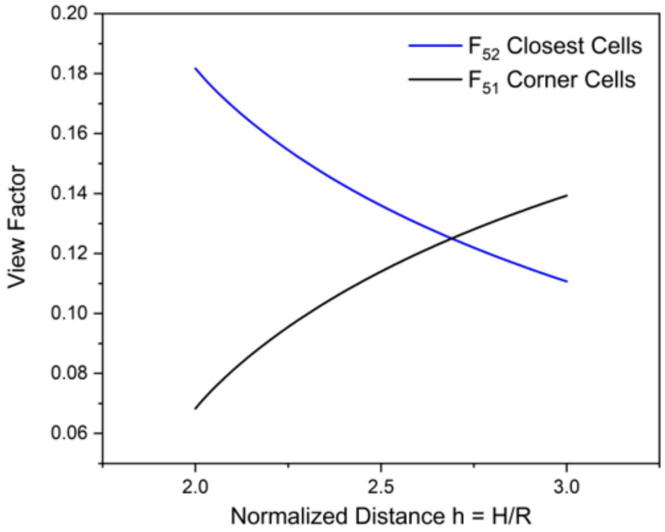

Figure 15. Comparison of view factors among different adjacent cells in orthogonal arrangement in Figure 14.

3.5. Effects of Radiation from Localized Hot Spots

It should be noted that the view factor for radiation heat flux calculation is based on the assumption that Cell 5 has a uniform surface temperature. Under certain conditions, the presence of localized hot spots may result in a non-uniform battery surface temperature, which may complicate the nature of radiative heat transfer. In such a case, the problem is no longer symmetric, similar to the one discussed in the previous sub-section. Therefore, radiative heat flux to each cell must be calculated separately. In order to investigate such effects, localized hot spots are introduced as shown in Figure 14, represented by the blue arc segment on the surface of Cell 5. The size of the hot spot is characterized by the angle φ shown in Figure 14, while the center of the hot spot is located along the center line of Cells 5 and 2. This hot spot is assigned a representative temperature of 750 K, while the rest part of Cell 5 is assumed to be at 300 K. A cell-to-cell gap of 1 mm is assumed. As we change the hot spot size, it is expected that both the radiative surface area and the view factor will vary accordingly.

Figure 16 shows the radiative heat flux per unit receiving surface area for hot spot sizes of 20°, 45°, 90° and 360°. In the 360° case, we observe that each radiative heat flux on Cells 2, 4, 6, and 8 accounts for 17% of the total radiation and that each radiative heat flux on Cells 1, 3, 7, and 9 accounts for 8%, consistent with their corresponding view factors shown in Figure 15. With a reduced hot spot size to 90°, more than 60% of the total radiation is received by Cell 2, the closest one to the hot spot, with a similar radiation heat flux on Cell 2 to the 360°case. With further reduced hot spot sizes to 45° and 20°, the radiation flux is reduced as expected: 80% and more radiation from the hot spot is directly emitted to the closest Cell 2. This shows that the nature of radiative heat transfer between cells, and, thus, the nature of thermal runaway propagation depends on the size of the hot spot. Mitigation strategies, therefore, must account for the nature of the hot spots expected.

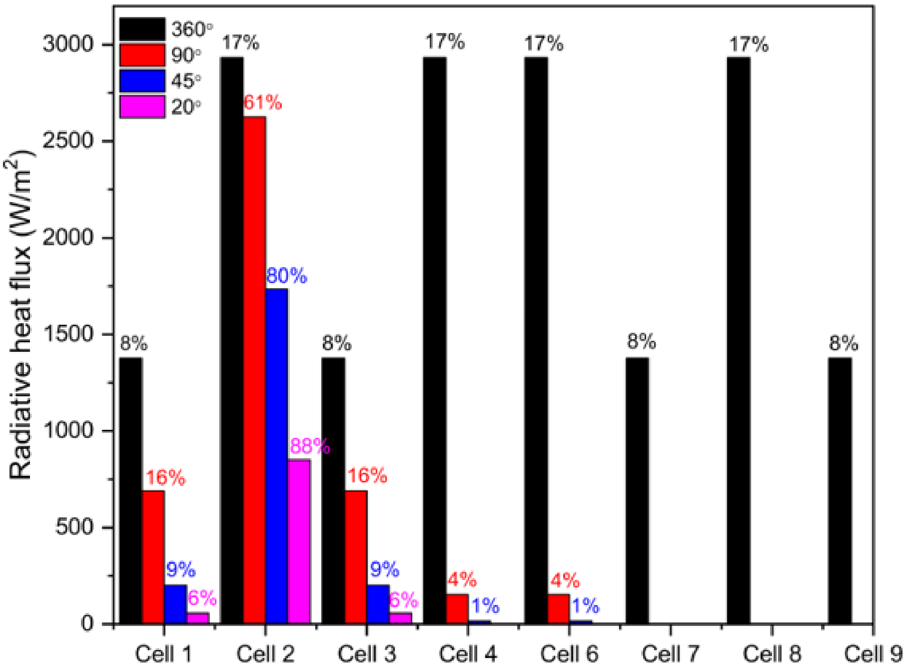

Figure 16. Radiation heat flux in an orthogonal 3×3 battery array with localized hot spot.

In the limiting case of an infinitely small hot spot, it can be shown that the view factor from the hot spot to an adjacent circle degenerates to R/H. This theoretical result can be applicable to highly localized hot spots, such as small, hot particles from venting events.

4. Conclusions

Based on carefully designed and validated calculations and numerical simulation, the interplay between radiation and pre-runaway chemistry in battery thermal runaway propagation is identified in the current study. Results evaluate the role of radiative heat transfer from a hot trigger cell to colder neighboring cells in the propagation of thermal runaway.

Results indicate that radiation-induced thermal runaway exhibits intrinsic differences between low and high trigger temperature regimes; at high triggering temperatures, thermal runaway is triggered very rapidly and close to the battery surface, and the thermal runaway reactions occur simultaneously in space and time. In this case, radiation plays a solely dominant and direct role. In contrast, at a low trigger temperature, thermal runaway is triggered much more slowly and deeper in the cell, and the thermal runaway reactions can separate in spatial and temporal domains due to the depletion of certain species.

By investigating the evolution of the net radiation flux during thermal runaway, we have found that the net radiation heat flux has a cross-over instant, beyond which the net radiation heat flux becomes negative. Therefore, radiation can either facilitate or mitigate thermal runaway. For high temperature conditions, the cross-over state is very close to the onset of thermal runaway—as such, radiation constantly facilities thermal runaway. In contrast, under low temperature conditions, the cross-over state can be far ahead of the onset of thermal runaway; therefore, radiation facilitates thermal runaway in the earlier stage and mitigates thermal runaway in the later stage.

Results from this work identify the non-monotonic role of radiation in thermal runaway triggering and provide direct insights into the complex interaction of two highly nonlinear phenomena: radiation heat transfer and chemical reactions during thermal runaway. The time-integrated radiation heat flux exhibits a non-monotonic dependence on the triggering temperature. The underlying reasons can be twofold: for one thing, the delay time of thermal runaway is substantially longer for low temperature conditions, albeit with a lower radiation heat flux; for another, the pre-runaway chemistry plays an increasingly significant role in increasing the battery temperature under lower triggering temperature conditions, which must be considered for radiation-induced thermal runaway propagation.

We analytically evaluated the view factor, accounting for the equal-spaced homogenous arrangement and the orthogonal arrangement of cells in practical battery packs. It was shown that the blocking effect in the equally spaced homogenous arrangement can decrease the radiation heat flux by as much as 8.2%. While in the orthogonal arrangement, a threshold cell separation distance exists, within which the closest cells receive higher radiation while beyond which the corner batteries receive higher radiation. The results indicate that radiation-induced thermal runaway propagation in a pack is not necessarily along the trajectory among closest cells. Radiation effects from a localized hot spot with varying sizes were also investigated, showing the increased focusing effects and necessitating specific thermal runaway prevention methods.

In the context of relatively little past work on radiative heat transfer during thermal runaway propagation, this work makes fundamental contributions in understanding the role of radiation and its interplay with chemical reactions that cause thermal runaway. The insights gained from this work may help develop strategies for reduced thermal runaway propagation and, hence, safer battery packs.

Author Contributions: Conceptualization, P.Z. and A.J.; methodology, P.Z., H.G. and L.Z.; software, L.Z.; validation, P.Z., H.G. and A.J.; formal analysis, P.Z. and L.Z.; investigation, P.Z., Y.C. and L.Z.; resources, P.Z. and L.Z.; data curation, Y.C. and L.Z.; writing—original draft preparation, P.Z. and L.Z.; writing—review and editing, H.G., Y.C. and A.J.; visualization, P.Z. and L.Z.; supervision, P.Z.; project administration, P.Z.; funding acquisition, P.Z. All authors have read and agreed to the published version of the manuscript.

Funding: This research is partially supported by the Ford Motor Company.

Institutional Review Board Statement: Not applicable.

Informed Consent Statement: Not applicable.

Data Availability Statement: Data involved in the paper will be provided upon request.

Acknowledgments: PZ appreciates the support of the Ford Motor Company.

Conflicts of Interest: The authors declare no conflict of interest. The funders had no role in the design of the study; in the collection, analyses, or interpretation of data; in the writing of the manuscript; or in the decision to publish the results.

References

1. National Blueprint for Lithium Batteries, 2021–2030, US Department of Energy. Available online: https://www.energy.gov/eere/vehicles/articles/national-blueprint-lithium-batteries (accessed on 13 July 2023).
2. Huang, Z.; Liu, J.; Zhai, H.; Wang, Q. Experimental investigation on the characteristics of thermal runaway and its propagation of large-format lithium ion batteries under overcharging and overheating conditions. *Energy* **2021**, *233*, 121103. [CrossRef]
3. Duh, Y.S.; Theng, J.H.; Chen, C.C.; Kao, C.S. Comparative study on thermal runaway of commercial 14500, 18650 and 26650 LiFePO4 batteries used in electric vehicles. *J. Energy Storage* **2020**, *31*, 101580. [CrossRef]
4. Ren, D.; Feng, X.; Liu, L.; Hsu, H.; Lu, L.; Wang, L.; He, X.; Ouyang, M. Investigating the relationship between internal short circuit and thermal runaway of lithium-ion batteries under thermal abuse condition. *Energy Storage Mater.* **2021**, *34*, 563–573. [CrossRef]
5. Liu, L.; Feng, X.; Zhang, M.; Lu, L.; Han, X.; He, X.; Ouyang, M. Comparative study on substitute triggerring approaches for internal short circuit in lithium-ion batteries. *Appl. Energy* **2020**, *259*, 114143. [CrossRef]
6. Huang, Z.; Li, H.; Mei, W.; Zhao, C.; Sun, J.; Wang, Q. Thermal Runaway Behavior of Lithium Iron Phosphate Battery during Penetration. *Fire Technol.* **2020**, *56*, 2405–2426. [CrossRef]
7. Xu, J.; Mei, W.; Zhao, C.; Liu, Y.; Zhang, L.; Wang, Q. Study on thermal runaway mechanism of 1000 mAh lithium ion pouch cell during nail penetration. *J. Therm. Anal. Calorim.* **2021**, *144*, 273–284. [CrossRef]
8. Ren, D.; Liu, X.; Feng, X.; Lu, L.; Ouyang, M.; Li, J.; He, X. Model-based thermal runaway prediction of lithium-ion batteries from kinetics analysis of battery components. *Appl. Energy* **2018**, *228*, 633–644. [CrossRef]
9. Gong, J.; Wang, Q.; Sun, J. Thermal analysis of nickel cobalt lithium manganese with varying nickel content used for lithium-ion batteries. *Thermochim. Acta* **2017**, *655*, 176–180. [CrossRef]
10. Lei, B.; Zhao, W.; Ziebert, C.; Uhlmann, N.; Rohde, M.; Seifert, H.J. Experimental Analysis of Thermal Runaway in 18650 Cylindrical Li-Ion Batteries Using an Accelerating Rate Calorimeter. *Batteries* **2017**, *3*, 14. [CrossRef]
11. Zhao, C.; Wang, T.; Huang, Z.; Wu, J.; Zhou, H.; Ma, M.; Xu, J.; Wang, Z.; Li, H.; Sun, J.; et al. Experimental study on thermal runaway of fully charged and overcharged lithium-ion batteries under adiabatic and side-heating test. *J. Energy Storage* **2021**, *38*, 102519. [CrossRef]
12. Hatchard, T.D.; MacNeil, D.D.; Basu, A.; Dahn, J.R. Thermal model of cylindrical and prismatic lithium-ion batteries. *J. Electrochem. Soc.* **2001**, *148*, A755–A761. [CrossRef]
13. Wang, Y.; Ren, D.; Feng, X.; Wang, L.; Ouyang, M. Thermal kinetics comparison of delithiated LiNMC cathodes. *J. Power Sources* **2021**, *514*, 230582. [CrossRef]
14. Xu, J.; Lan, C.; Qiao, Y.; Ma, Y. Prevent thermal runaway of lithium-ion batteries with minichannel cooling. *Appl. Therm. Eng.* **2017**, *110*, 883–890. [CrossRef]
15. Offer, G.; Patel, Y.; Hales, A.; Diaz, L.; Marzook, M. Cool metric for lithium-ion batteries could spur progress. *Nature* **2020**, *582*, 485–487. [CrossRef]
16. Yan, W.; Wang, Z.; Ouyang, D.; Chen, S. Analysis and prediction of thermal runaway propagation interval in confined space based on response surface methodology and artificial neural network. *J. Energy Storage* **2022**, *55*, 105822. [CrossRef]
17. Zhu, Y.; Wang, Z.; Bian, H.; Wang, J.; Bai, W.; Gao, T.; Bai, J.; Zhou, Y. Critical conditions for the thermal runaway propagation of lithium-ion batteries in air and argon environments. *J. Therm. Anal. Calorim.* **2022**, *147*, 13699–13710. [CrossRef]
18. Wang, Z.; Wang, K.; Wang, J.; Yang, Y.; Zhu, Y.; Bai, W. Inhibition effect of liquid nitrogen on thermal runaway propagation of lithium ion batteries in confined space. *J. Loss. Prev. Process Ind.* **2022**, *79*, 104853. [CrossRef]
19. Zhao, P.; Garcia, A.; Burton, T. Initiation and propagation of curved reaction front in solids: In-sights into solid combustion and battery thermal runaway, Combust. *Flame* **2022**, *238*, 111951. [CrossRef]
20. Ren, D.; Feng, X.; Lu, L.; Ouyang, M.; Zheng, S.; Li, J.; He, X. An electrochemical-thermal coupled overcharge-to-thermal-runaway model for lithium-ion battery. *J. Power Sources* **2017**, *364*, 328–340. [CrossRef]
21. Jia, Z.; Qin, P.; Li, Z.; Wei, Z.; Jin, K.; Jiang, L.; Wang, Q. Analysis of gas release during the pro-cess of thermal runaway of lithium-ion batteries with three different cathode materials. *J. Energy Storage* **2022**, *50*, 104302. [CrossRef]
22. Mishra, D.; Shah, K.; Jain, A. Investigation of the impact of flow of vented gas on propagation of thermal runaway in a Li-ion battery pack. *J. Electrochem. Soc.* **2021**, *168*, 060555. [CrossRef]
23. Wang, Q.; Huang, P.; Ping, P.; Du, Y.; Li, K.; Sun, J. Combustion behavior of lithium iron phosphate battery induced by external heat radiation. *J. Loss Prev. Process Ind.* **2017**, *49*, 961–969. [CrossRef]
24. Wang, Z.; He, T.; Bian, H.; Jiang, F.; Yang, Y. Characteristics of and factors influencing thermal runaway propagation in lithium-ion battery packs. *J. Energy Storage* **2021**, *41*, 102956. [CrossRef]
25. Hatchard, T.D.; MacNeil, D.D.; Stevens, D.A.; Christensen, L.; Dahn, J.R. Importance of heat transfer by radiation in li-ion batteries during thermal abuse. *Electrochem. Solid-State Lett.* **2000**, *3*, 305. [CrossRef]
26. Fang, J.; Cai, J.; He, X. Experimental study on the vertical thermal runaway propagation in cylindrical Lithium-ion batteries: Effects of spacing and state of charge. *Appl. Therm. Eng.* **2021**, *197*, 117399. [CrossRef]
27. Tang, Z.; Song, A.; Wang, S.; Cheng, J.; Tao, C. Numerical Analysis of Heat Transfer Mechanism of Thermal Runaway Propagation for Cylindrical Lithium-ion Batteries in Battery Module. *Energies* **2020**, *13*, 1010. [CrossRef]
28. Yan, W.; Wang, Z.; Chen, S. Quantitative analysis on the heat transfer modes in the process of thermal runaway propagation in lithium-ion battery pack under confined and semi-confined space. *Int. J. Heat Mass Transf.* **2021**, *176*, 121483. [CrossRef]

29. Allafi, W.; Zhang, C.; Uddin, K.; Worwood, D.; Dinh, T.Q.; Ormeno, P.A.; Li, K.; Marco, J. A lumped thermal model of lithium-ion battery cells considering radiative heat transfer. *Appl. Therm. Eng.* **2018**, *143*, 472–481. [CrossRef]
30. Lopez, C.F.; Jeevarajan, J.A.; Mukherjee, P.P. Experimental analysis of thermal runaway and propagation in Li-ion battery modules. *J. Electrochem. Soc.* **2015**, *162*, A1905. [CrossRef]
31. Mishra, D.; Jain, A. Multi-mode heat transfer simulations of the onset and propagation of thermal runaway in a pack of cylindrical Li-ion batteries. *J. Electrochem. Soc.* **2021**, *168*, 020504. [CrossRef]
32. Feng, X.; Lu, L.; Ouyang, M.; Li, J.; He, X. A 3D thermal runaway propagation model for a large format lithium ion battery module. *Energy* **2016**, *115*, 194–208. [CrossRef]
33. Mishra, D.; Shah, K.; Jain, A. Investigation of the Impact of Radiative Shielding by Internal Partitions Walls on Propagation of Thermal Runaway in a Matrix of Cylindrical Li-Ion Cells. *J. Electrochem. Soc.* **2021**, *168*, 120507. [CrossRef]
34. Zhang, L.; Yang, S.; Liu, L.; Zhao, P. Cell-to-cell variability in Li-ion battery thermal runaway: Experimental testing, statistical analysis, and kinetic modeling. *J. Energy Storage* **2022**, *56*, 106024. [CrossRef]
35. Zhang, L.; Zhao, P.; Xu, M.; Wang, X. Computational identification of the safety regime of Li-ion battery thermal runaway. *Appl. Energy* **2020**, *261*, 114440. [CrossRef]
36. Zhao, P.; Liu, L.; Zhang, L.; Chen, Y. Mitigating battery thermal runaway through mild combustion. *Chem. Eng. J. Adv.* **2022**, *9*, 100208. [CrossRef]
37. Bergman, L.; Incropera, F.P.; DeWitt, D.P.; Lavine, A.S. *Fundamentals of Heat and Mass Transfer*; Wiley: New York, NY, USA, 2011.
38. Fan, L.; Khodadadi, J.M.; Pesaran, A.A. A parametric study on thermal management of an air-cooled lithium-ion battery module for plug-in hybrid electric vehicles. *J. Power Sources* **2013**, *238*, 301–312. [CrossRef]
39. Coleman, B.; Ostanek, J.; Heinzel, J. Reducing cell-to-cell spacing for large-format lithium ion battery modules with aluminum or PCM heat sinks under failure conditions. *Appl. Energy* **2016**, *180*, 14–26. [CrossRef]
40. Jia, Y.; Uddin, M.; Li, Y.; Xu, J. Thermal runaway propagation behavior within 18650 lithium-ion battery packs: A modeling study. *J. Energy Storage* **2020**, *31*, 101668. [CrossRef]